Mon. Not. R. Astron. Soc. **384,** 316–322 (2008) doi:10.1111/j.1365-2966.2007.12705.x

An infrared study of the double nucleus in NGC 3256

P. Lira,[1⋆] V. Gonzalez-Corvalan,[1,2] M. Ward[3] and S. Hoyer[1]

[1]*Departamento de Astronomía, Universidad de Chile, Casilla 36-D, Santiago, Chile*
[2]*Department of Astronomy and Astrophysics, UC Santa Cruz, 201 Interdisciplinary Sciences Building, Santa Cruz, CA 95064, USA*
[3]*Department of Physics, University of Durham, Science Laboratories, South Road, Durham DH1 3LE*

Accepted 2007 November 9. Received 2007 November 9; in original form 2007 August 30

ABSTRACT

We present new resolved near- and mid-infrared (mid-IR) imaging and *N*-band spectroscopy of the two nuclei in the merger system NGC 3256, the most IR luminous galaxy in the nearby Universe. The results from the spectral energy distribution fit to the data are consistent with previous estimates of the amount of obscuration towards the nuclei and the nuclear star formation rates. However, we also find substantial differences in the infrared emission from the two nuclei which cannot be explained by obscuration alone. We conclude that the northern nucleus requires an additional component of warm dust in order to explain its properties. This suggests that local star-forming conditions can vary significantly within the environment of a single system.

Key words: galaxies: general – galaxies: nuclei.

1 INTRODUCTION

The dominance of obscured star formation in the early Universe makes the dusty nearby systems interesting laboratories in which to probe their physics and evolution. Because of their high level of obscuration, such studies are well suited to observations at near- and mid-infrared (near-IR) wavelengths. Our understanding of these sources has improved considerably since the *IRAS* era of the 1980s. This is partly due to the results from *Infrared Space Observatory* (*ISO*) in the 1990s and most recently from *Spitzer*. However, high spatial resolution is still not attainable from space facilities. This situation is, however, rapidly changing with the advent of new ground-based instrumentation which is a valuable complement to the space missions.

Because of its closeness ($D \sim 39$ Mpc, for $H_\circ = 70\,\mathrm{km\,s^{-1}\,Mpc^{-1}}$) and luminosity ($L_{\rm bol} \sim L_{\rm IR} \sim 6 \times 10^{11}\,\mathrm{L_\odot}$), NGC 3256 is one of the best-studied Luminous Infrared Galaxies (LIRGs) and it is very close to the luminosity range of Ultraluminous Infrared Galaxies. Its powerful IR emission is the result of a merger of two massive galaxies, whose nuclei have a projected separation of only ∼1 kpc, indicating an advanced stage of the collision.

NGC 3256 is also amongst the most X-ray luminous galaxies for which there is no clear evidence of the presence of a (luminous) active nucleus. In fact, the estimated luminosity of NGC 3256 ($L_{\rm x} \sim 10^{42}$ erg s^{-1} in the 0.5–10 keV band – Moran, Lehnert & Helfand 1999; Lira et al. 2002) is consistent with the maximum limit normally adopted to separate active galactic nuclei (AGN) from starburst galaxies found in deep X-ray surveys (see Alexander et al. 2005, and references therein).

⋆E-mail: plira@das.uchile.cl

In this paper, we present a study of the near- and mid-IR resolved emission from the two nuclei in the prototype LIRG NGC 3256. In Section 2, we describe the high spatial resolution, ground-based observations obtained in the *N*-band. In Sections 3 and 4, the details of our data analysis are presented. In Section 5, the Spectral Energy Distribution (SED) of NGC 3256 is explored using our new *N*-band data, plus observations extracted from the literature and *Spitzer* and *Hubble Space Telescope* (*HST*) archival images. Finally, the discussion of our results is presented in Section 6.

2 OBSERVATIONS AND DATA REDUCTION

2.1 Imaging

The high-resolution *N*-band imaging of NGC 3256 was obtained with the Thermal Infrared MultiMode Instrument (TIMMI2) camera on the European Southern Observatory (ESO) 3.6-m telescope at La Silla on 2001 February 24. A narrow *N*-band filter was used ($\lambda_{\rm c} \sim 11.5\,\mu$m ; $\Delta\lambda \sim 1.2\,\mu$m), and the image scale was 0.2 arcsec per pixel. Standard chopping and nodding techniques were employed with perpendicular chop and nod throws of 15 arcsec. Despite the highly peaked light distribution centred on the nuclear region, it is expected that some galactic emission is also present ∼15 arcsec away from the nuclear sources. This might affect our ability to obtain an accurate sky subtraction, and is discussed further in Section 3.

The final image was constructed by shifting each individual frame on to a common reference position determined by using the centroid of the central source. The resulting exposure time was 1.16 ks. This image was flux calibrated using standard stars observed throughout the night. These showed an RMS error of 8 per cent in their fluxes. Inspection of the radial profile of the standard stars showed that

the observations were diffraction-limited with a full width at half-maximum (FWHM) ∼0.8 arcsec.

An uncalibrated, *N*-band 10.5 μm image of NGC 3256 was published by Böeker et al. (1997) as one of the first science images obtained with the Mid and Near Infrared Array Camera (MANIAC) camera. Siebenmorgen, Krügel & Spoon (2004) presented 8.6 and 10.4 μm imaging of this galaxy obtained with TIMMI2, but the detection of the southern nucleus is not discussed. Alonso-Herrero et al. (2006) have recently published a narrow band, 8.7 μm image of NGC 3256 and their measurements of the northern and southern nuclei will be used later in Section 5. We have also analysed archival *Spitzer* images of NGC 3256 (principal investigator, Fazio). These observations were carried out with the Infrared Array Camera (IRAC) camera in 2004 June. The 'Post Basic Calibrated Data' were used to determine the photometry of the nuclei. Saturation affected the northern nucleus in the 8 μm band images, and so these were not used. Finally, for the northern nucleus we also extracted the archival *HST* observations obtained using the WFPC2 camera with the F300W, F555W and F814W filters during 2001 June and August (PI's, Windhorst and van der Marel). We did not include the optical data published by Lípari et al. (2000) in our analysis because the used apertures and seeing conditions did not meet our requirements (see Section 5).

2.2 Spectroscopy

Long-slit *N*-band spectroscopy of NGC 3256 was obtained during the science verification phase of the TReCS camera on Gemini South on 2004 January 3. The low-resolution KBrC grating was used giving a spectral resolution $R \sim 100$ in the 8–12.5 μm wavelength range. The slit width was 1.3 arcsec, and was rotated to a nearly north–south position angle in order to cover both nuclei simultaneously. The chopping and nodding were performed in the direction perpendicular to the slit orientation, with a throw of 30 arcsec. The total on-source integration time was 1.28 ks.

The images were reduced using the Gemini mid-IR IRAF package, which derives background-subtracted images from different chopping and nodding positions, then registers them and produces a final averaged image. Extraction of the spectra of both nuclei was performed using standard IRAF package routines. Due to the low-signal-to-noise ratio (S/N) available for the southern nucleus, we used the trace function determined for the northern nucleus to extract this spectrum. Aperture photometry of the TIMMI2 image within a diameter of 1.3 arcsec has been used to determine a good absolute flux calibration for the spectra.

Spitzer IRS observations of NGC 3256 have been published by Brandl et al. (2006) and are included in our analysis (Section 5). The observations were carried out on the 2004 May 13 using the low-resolution module ($R \sim 65$–130). The slit widths were ∼3.6 arcsec in the 5–15 μm range and ∼10.5 arcsec for wavelengths greater than 15 μm, although the final flux calibration was obtained through the widest slit. Also, Martín-Hernández et al. (2006) have recently presented spatially resolved 7.5–13.9 μm spectroscopy of the double nuclei in NGC 3256 obtained with TIMMI2. Finally, Siebenmorgen et al. (2004) presented TIMMI2 and *ISO* spectroscopy for this galaxy, but as was the case with their TIMMI2 imaging, there is no discussion of the possible detection of the southern nucleus.

3 IMAGE ANALYSIS

Fig. 1 shows the TIMMI2 observations of the nuclear region in NGC 3256. The emission is clearly dominated by a central extended source, although other clumps of emission can be seen distributed around it. We identify the central source with the northern nucleus, while the much fainter source located ∼5 arcsec to the south, corresponds to the southern nucleus.

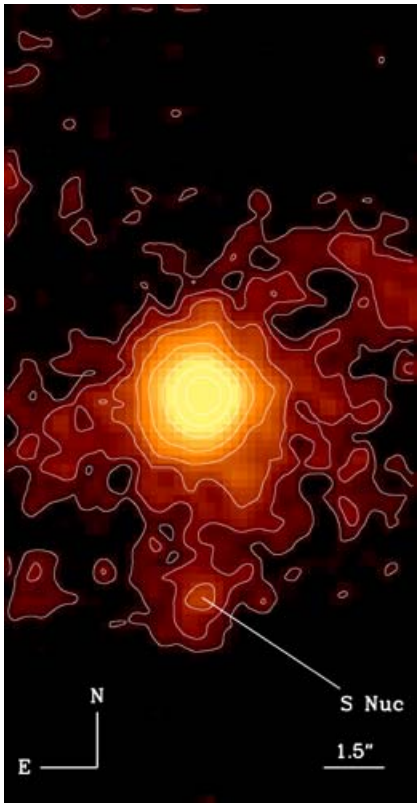

Figure 1. The high-resolution narrow *N*-band image ($\lambda_c \sim 11.5$ μm) of the central region of NGC 3256 observed using TIMMI2. This image has been smoothed and displayed on a logarithmic scale. Clearly, the emission is dominated by the northern nucleus, but the southern nucleus is also detected.

The radial profiles of both nuclei are shown in Fig. 2. The northern nucleus is clearly extended when compared with a stellar point spread function. A best fit to its profile was obtained by using a combination of an exponential and a Lorentzian function. In order to reduce contamination from the northern nucleus in the photometry of the southern source, its profile was derived using photometry obtained from the lower half of the circular apertures centred on this source. Despite the much lower S/N, it is clearly seen that the southern nucleus is also well resolved. Furthermore, the same fit that described the profile of the northern nucleus is also found to provide a good representation of the southern source. In fact the *HST*-Near Infrared Camera and Multi Object Spectrometer (NICMOS) images show that the southern nucleus is the more extended of the two nuclei at near-IR wavelengths (Lira et al. 2002).

Photometry calculated within an aperture of 3 arcsec diameter centred on the northern and the southern nuclei gives fluxes of ∼0.8 and ∼0.1 Jy, respectively (see Table 1). Despite our efforts to reduce the contamination from the northern nucleus in the southern aperture, we must consider the flux from the southern nucleus to be uncertain. The total emission within an aperture of 9.5 arcsec in diameter centred on the northern peak corresponds to 1.8 Jy. However, since the background subtraction of the image was obtained using a chopping throw of only 15 arcsec, it is important to quantify the possibility of sky oversubtraction which could affect these measurements.

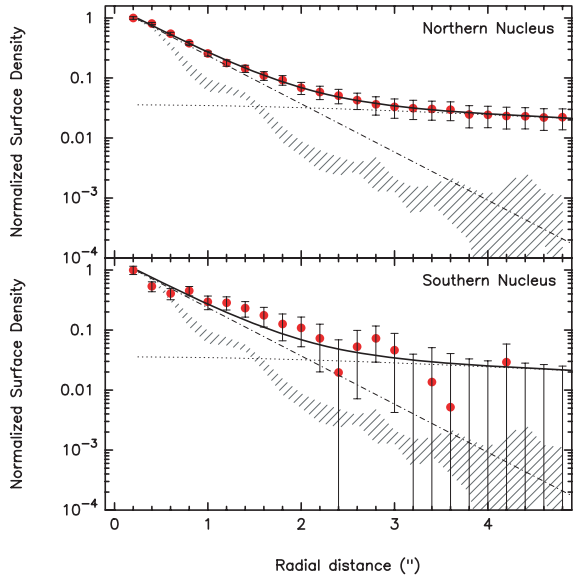

Figure 2. Normalized radial profiles of the two nuclei in NGC 3256. The profile of the southern nucleus was derived by using the lower half of the circular apertures centred on the nucleus, in order to avoid the strong contamination from the northern source. A 1σ interval in radial profiles of the standard stars observed during the same night are also included for comparison (hashed region). The extended profile of the northern nucleus was fitted using the sum of a Lorentzian and exponential function (shown as a thin continuous line). The same fit is superimposed on the profile of the southern nucleus.

The total emission measured from the TIMMI2 image can be compared with the *IRAS* 12 μm ($\Delta\lambda = 8.5$–15 μm) photometry obtained by Sanders et al. (1995). For an *IRAS* beam of 0.77 arcmin in diameter they measured a marginally resolved source with a total flux of 3.6 Jy, which corresponds to a corrected flux of ∼5 Jy in the 10.9–12.1 μm TIMMI2 band, if the northern nucleus best-fitting model presented in Section 5 is adopted, and this model is representative of the emission from the whole region. Hence, the *IRAS* observations provide an estimate of the size of the total emitting region, which is comparable to the *IRAS* beam.

If we assume that the differences between the *IRAS* and the TIMMI2 fluxes are due to emission evenly distributed within an annular region of the inner and the outer diameters 9.5 arcsec and 0.77 arcmin, respectively, then the corresponding surface brightness would be ∼2 mJy arcsec^{-2}. This would correspond to corrections of ∼2, ∼ 15 and ∼10 per cent, respectively, to the fluxes for the total, northern and southern regions presented in Table 1 (see three last entries). However, it is quite possible that the emission from outside the TIMMI2 image does not follow a completely even distribution, but instead has a steep profile. To test this scenario, we extrapolated the fitted profile shown in Fig. 2 out to the region used for the sky subtraction (∼15 arcsec away). The estimated value is only ∼0.3 mJy arcsec^{-2}. Again, this result suggests that our measurements do not suffer from a severe background oversubtraction. Integrating the fit to the profile of the northern nucleus out to a diameter of 0.77 arcmin underestimates the observed *IRAS* flux by ∼60 per cent, suggesting that the larger scale surface brightness (i.e. that lying outside the TIMMI2 image) is actually closer to the flat distribution that we proposed earlier.

Fig. 3 presents the IRAC images in the 3.6, 4.5 and 5.8 μm bands. The spatial resolution of IRAC (FWHM ∼1.5 arcsec) clearly separates the two nuclei. It can be seen that in the 4.5 μm band image the two nuclei have a very similar peak brightness, while the northern nucleus is more prominent at 3.6 and 5.8 μm.

Ptak et al. (2006) and Taylor-Mager et al. (2007) have recently presented the archival WFPC2 data used in this work to obtain the optical photometry for the northern nucleus. Also, a spectacular WFPC2 colour image of NGC 3256 can be found in Zepf et al. (1999).

The TIMMI2, IRAC and WFPC2 photometry is given in Table 1. The IRAC photometry was obtained in apertures that roughly correspond to the same spatial region as measured in the 3.0 arcsec TIMMI2 aperture photometry. This was achieved by deconvolving the TIMMI2 image of the northern nucleus (using a standard star observation) and then convolving it with the characteristic FWHM for each IRAC band. Finally, an aperture size was defined so that the same fractional flux as that measured from the TIMMI2 image would be obtained. We assumed that the same IRAC apertures apply for the photometry of the southern nucleus. Given the small FWHM of the WFPC2 camera (∼0.15 arcsec), a 3.0 arcsec aperture was

Table 1. Aperture photometry of the two nuclei in NGC 3256. Errors correspond to 2 per cent for the WFPC2, 15 per cent for the IRAC and 8 per cent for the TIMMI2 measurements. Kotilainen et al. (1996) report errors of 5 per cent for JHK' and 10 per cent for the L'-band photometry, respectively. See the text for details of the used apertures.

Wavelength	Aperture (arcsec)	North (mJy)	South (mJy)	Source/Reference
2924 Å	3.0	0.45 ± 0.01	–	WFPC2 F300W – this work
5252 Å	3.0	2.79 ± 0.06	–	WFPC2 F555W – this work
8269 Å	3.0	7.02 ± 0.14	–	WFPC2 F814W – this work
1.25 μm	3.0	21.6 ± 1.1	4.7 ± 0.2	Kotilainen et al. (1996)
1.65 μm	3.0	33.2 ± 1.7	9.0 ± 0.4	Kotilainen et al. (1996)
2.10 μm	3.0	33.7 ± 1.7	10.5 ± 0.5	Kotilainen et al. (1996)
3.6 μm	3.6	33.5 ± 5.0	16.8 ± 2.5	IRAC band-1 – this work
3.75 μm	3.0	32.3 ± 3.2	24.8 ± 2.5	Kotilainen et al. (1996)
4.5 μm	3.6	30.0 ± 4.5	26.0 ± 3.9	IRAC band-2 – this work
5.8 μm	4.0	128 ± 19	71 ± 11	IRAC band-3 – this work
8.74 μm	1.4*	230 ± 11	40 ± 3	Alonso-Herrero et al. (2006)
11.5 μm	1.3†	350 ± 28	26 ± 2	TIMMI2 – this work
11.5 μm	3.0	810 ± 65	86 ± 7	TIMMI2 – this work
11.5 μm	9.5	1800 ± 144	–	TIMMI2 – this work

* A factor of 1.4 is required to correct these fluxes to a ∼3.0 arcsec aperture.
† Used to derive the absolute calibration for the TReCS spectroscopy (see Fig. 4).

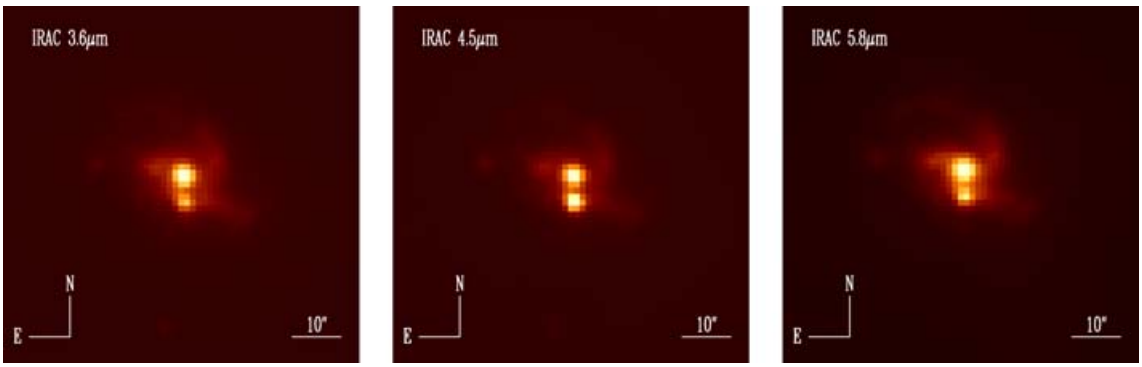

Figure 3. IRAC images of NGC 3256 in the 3.6, 4.5 and 5.8 μm bands.

directly applied to obtain the optical photometry for the northern nucleus.

4 SPECTRAL ANALYSIS

The *N*-band spectra of the northern and the southern nuclei in NGC 3256 are shown in Fig. 4. Both spectra are flanked by the rising PAH features at 7.7 μm and the narrow [Ne II]λ12.8 μm emission line which is blended with the 12.7 μm PAH feature. Unfortunately, the [Ne II]λ12.8 μm line is not completely covered in the spectral range of our data but it can be clearly seen in the data of Martín-Hernández et al. (2006).

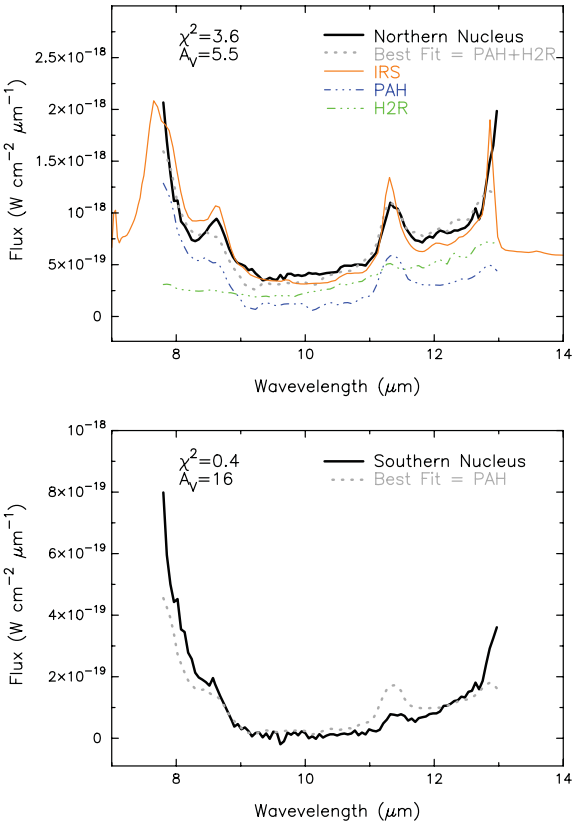

Figure 4. *N*-band spectra of the nuclei in NGC 3256. Absolute flux calibration was obtained using *N*-band photometry measured in 1.3 arcsec diameter apertures (see Table 1). The *Spitzer* IRS spectrum obtained by Brandl et al. (2006) is overplotted on the TReCS observations for the northern nucleus, after applying a scaling factor of 0.18.

The nuclear region of NGC 3256 was observed with the *Spitzer* IRS spectrograph. As can be seen in Fig. 4, the IRS spectrum is a very good match to the TReCS observations of the northern nucleus, which clearly dominates the emission in the mid-IR (see Fig. 1). Since the flux calibration of the IRS spectrum was obtained from a much larger aperture (10.5 arcsec), a scaling factor of 0.18 had to be applied to these data. This is also similar to the ratio between the 1.3 and 9.5 arcsec fluxes measured in the apertures applied to the TIMMI2 images, and presented in Table 1.

Following the model proposed by other authors (e.g. Laurent et al. 2000; Sturm et al. 2000), we assume a simple description of the *N*-band emission, and fitted the spectra of both nuclei as a combination of several components:

$$F_\lambda = \left\{ C_1 F_\lambda^{\mathrm{H\,II\,R}} + C_2 F_\lambda^{\mathrm{PAH}} + C_3 F_\lambda^{\mathrm{AGN}} \right\} \times 10^{-A_\lambda/2.5},$$

where $F^{\mathrm{H\,II}}$ and F^{PAH} are empirical templates of an H II region and a PAH-dominated PDR region (Peeters, Spoon & Tielens 2004). The F^{AGN} term is a template of a type 2 AGN, i.e., it corresponds to the reprocessed emission from the dusty torus without the directly visible contribution from an active nucleus. These templates were taken from Sturm et al. (2000) and Le Floc'h et al. (2001). A_λ is the assumed extinction curve. We have used the mid-IR extinction curves published by Draine (2003). C_1, C_2 and C_3 are free parameters which are determined by using χ^2 minimization and the σ spectrum, which is dominated by background emission.

Since the spectral range of our data is too narrow to allow us to determine the strength of the continuum, the PAH features and the extinction (which includes the silicate absorption at ∼9.8 μm), we have instead assumed a fixed value for the normalization of the extinction curve, (A_V). Since our spectra were obtained using a ∼1 arcsec slit, we have adopted $A_V = 5.5$ for the northern nucleus and $A_V = 16$ for the southern nucleus, as was determined from the 0.3 arcsec resolution NICMOS images (Lira et al. 2002). These values are rather uncertain, since they were determined by assuming an intrinsic $H - K$ colour for the starburst region. The same method gives $A_V = 2.5$ and 5.3 magnitudes for the northern and the southern nuclei, respectively, when the colours are measured from a 3 arcsec aperture, while the use of a correlation between the radio 6 cm and [Fe II] fluxes implies $A_V = 7.8$ and 10.7 for the northern and the southern nuclei, respectively (Kotilainen et al. 1996).

The outcome from the spectral fitting is summarized in Table 2. A clear result is that the northern nucleus shows a strong continuum contribution, while the southern nucleus is dominated by PAH emission, without the need for a significant continuum component. We

Table 2. Results from the spectral fitting. The percentage contributions of each component to the integrated 8–12.5 μm flux are presented.

Nucleus	χ^2	Fixed A_V	PAH	HIIR	AGN
North	3.6	5.5	∼55 per cent	∼45 per cent	0 per cent
South	0.4	16.0	100 per cent	0 per cent	0 per cent

Table 3. Flux and EW for the 11.3 μm PAH emission band.

Instrument	Slit (arcsec)	Flux ($\times 10^{-20}$ W cm^{-2})	EW (μm)	References
Northern nucleus				
TIMMI2	1.2	25	–	1
TReCS	1.3	17	0.3	2
TIMMI2	3.0	30	0.4	3
IRS	10.5	85	0.5	4
IRS	10.5	120	0.4	2
ISO	24.0	107	1.0	3
Southern nucleus				
TIIMI2	1.2	5	–	1
TRcES	1.3	2	0.7	2

References: (1) Martín-Hernández et al. (2006); (2) this work; (3) Siebenmorgen et al. (2004); (4) Brandl et al. (2006).

have explored adopting lower values of A_V when fitting the spectrum of the southern source. In particular, in Section 5, we derive an extinction of $A_V = 10$ for this nucleus. However, these changes have a very little impact on the best-fitting results.

Our fit suggests that the continuum of the northern nucleus has a stellar origin ($F^{\rm H\,II}$), although if only an AGN continuum is allowed for the fit, then the result is also acceptable ($\chi^2 \lesssim 4$). However, the presence of an AGN in NGC 3256 is not supported by the very considerable body of observational evidence which indicates that an active nucleus is not present in this galaxy, or at least if it exists at all it is not the main component responsible for the powerful IR and X-ray emission (Doyon, Joseph & Wright 1994; Moorwood & Oliva 1994; Norris & Forbes 1995; Kotilainen et al. 1996; Rigopoulou et al. 1996; Lípari et al. 2000; Lira et al. 2002; Verma et al. 2003).

We have also measured the flux and equivalent width of the 11.3 μm PAH feature clearly seen in both our spectra. Since it is not possible to easily unblend this emission from the neighbouring 12.7 μm PAH band and strong [Ne II]λ12.8 μm line, we have derived these measurements by simply assuming the continuum level to be a straight line from 10.9 to 11.7 μm. We compare our measurements with those from the literature in Table 3. In general, there is a good agreement between values obtained through similar slit widths, given the uncertainties in the absolute flux calibrations for spectroscopy and the different adopted continuum levels. In particular, we have re-analysed the IRS data using the continuum fit as defined above.

5 MODELLING THE SPECTRAL ENERGY DISTRIBUTION

In Fig. 5, we show the SEDs for the nuclei in NGC 3256. Optical WFPC2 photometry is presented for the northern nucleus only. For both nuclei, we have included near-IR fluxes from Kotilainen et al. (1996), the IRAC photometry, narrow-band Gemini-TReCS observations at 8.74 μm from Alonso-Herrero et al. (2006), and our new TIMMI2 observations.

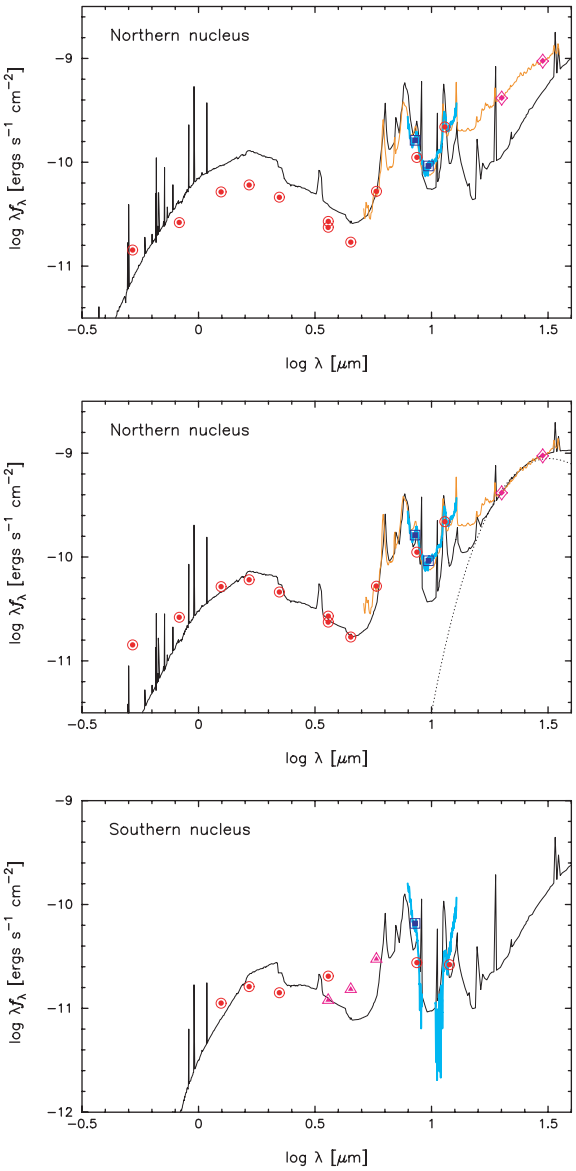

Figure 5. SED for the nuclei in NGC 3256. The top and middle panels show a fit to the northern nucleus (including a Grey-Body component in the middle panel – dotted line), while the lower panel shows a fit to the southern nucleus. Optical, near- and mid-IR aperture photometry is shown by circles (see Table 1). The mid-IR TReCS (and for the northern nucleus, IRS) spectra, scaled to the observed 3 arcsec diameter aperture TIMMI2 fluxes, are also shown with a thick and thin line, respectively. The spectra were binned to add further points to the SEDs (squares for TReCS data; diamonds for IRS data). Starburst models were taken from the work of Dopita et al. (2005).

For construction of the SEDs, we aimed to use fluxes obtained from a spatial region closely corresponding to the 3 arcsec diameter apertures used for our TIMMI2 imaging, which is characterized by a diffraction-limited FWHM ∼0.8 arcsec. This is already the case for the near-IR data taken from Kotilainen et al. (FWHM ∼0.8–1 arcsec). The WFPC2 and IRAC photometry presented in Section 3 also correspond to effective 3 arcsec diameter apertures. Similar to the analysis performed to determine the IRAC photometry, we estimate that a factor of 1.4 is necessary to correct the photometry

presented in Alonso-Herrero et al. using a 1.4 arcsec diameter aperture (with a resolution of ∼0.3 arcsec) to 3 arcsec. All results from the aperture photometry are presented in Table 1.

The TReCS spectra are overplotted on the SEDs in Fig. 5 after scaling them to the TIMMI2 flux observed in a 3 arcsec aperture (see Table 1). The IRS spectrum was included only for the northern nucleus after applying a scaling factor of 0.44. Given the good match between the TReCS and IRS spectra in the 8–12.5 μm wavelength range (see Fig. 4), we have assumed that the northern nucleus is also responsible for most of the IRS flux at wavelengths longer than 13 μm. As discussed before, all photometric measurements were corrected to correspond to fluxes predicted within a ∼3 arcsec aperture.

Kotilainen et al. (1996) showed that the southern nucleus becomes relatively more prominent at longer wavelengths, and is comparable to the northern nucleus in the *L*-band. They interpreted this difference as being due to different amounts of dust obscuration towards the two nuclei. However, our *N*-band data show a very weak southern nucleus when compared with the northern source, which is not consistent with such an explanation. In addition, the IRAC observations presented in Fig. 3 confirm this trend. The measured fluxes clearly show that their emission is very nearly the same at ∼4.5 μm, but diverge longwards and shortwards of this wavelength (see Table 1).

We performed an unweighted fit to the SEDs using the models presented by Dopita et al. (2005), which include a self-consistent treatment of dust re-emission from a starburst region. We also added extinction from a foreground screen of dust which was parametrized using the Calzetti et al. (2000) extinction law, ranging from the optical to 2.2 μm, and the Draine (2003) extinction curves from 2.2 μm longwards. The best-fitting models imply visual band extinctions of ≈5 and ≈10 mag for the northern and the southern nuclei, respectively. This is in good agreement with the previous determinations discussed in Section 4 within the uncertainties. These are mainly due to the assumption that a screen of foreground dust can account for the extinction towards the nuclei all the way from the optical to the mid-IR, since the geometry of these regions is probably more complex. Also, the adoption of a particular extinction curve would have some impact on the final determined extinction, while the templates used in our description of the spectra might not properly describe the intrinsic emission.

The starburst models have two free parameters, the ISM pressure (with $P/k = 10^4$, 10^6 and 10^7 cm^{-3} K) and the characteristic timescale for the 'clearing' of the star-forming regions (i.e. the time required for the covering factor of the star-forming clouds to decrease from 0.9 to 0.1). Changes in the pressure affect the model SEDs for fluxes above ∼15 μm, and therefore are not well constrained by our SED data. However, Rigopoulou et al. (1996) have determined an electron density ∼300–400 cm^{-3} for the central region in NGC 3256, and therefore we considered those SED models corresponding to $P/k = 10^{6-7}$ cm^{-3} K. The best-fitting models imply clearing times between 16 and 32 Myr for both nuclei.

Generally, the starburst models provide a good match to the SEDs. The northern nucleus, however, clearly requires an extra component in its continuum at $\gtrsim$10 μm, as can be seen by comparing the top and the middle panels in Fig. 5. This is in agreement with our findings from the spectral analysis. The reprocessing of emission absorbed by foreground dust is not expected to contribute significantly at these wavelengths as the characteristic temperature of this emission would be lower than 50 K. Instead, we have modelled the excess flux as a Grey body assuming an emissivity with index $\beta = -1.5$. The best-fitting temperature for this component is ∼80 K. The origin of this emission could be explained if the actual distribution of dust grain sizes is different to the one used in Dopita's models. If this interpretation is correct then the excess emission is due to a comparatively larger contribution from very small dust grains, which dominate the dust re-emission in the mid-IR (Désert et al. 1990).

6 DISCUSSION

The normalization of the starburst SED models allows us to infer a star formation rate (SFR) of ∼15 and ∼6 $M_\odot$ yr^{-1} for the northern and the southern nuclei, respectively. This estimation does not take into account the Grey-body component added to the fit of the northern nucleus since its integrated luminosity corresponds to $\lesssim$25 per cent of the total emission. These SFRs are in good agreement with the values obtained using the supernova rate of 0.3 yr^{-1} per nucleus derived from radio observations (Norris & Forbes 1995) by assuming a conversion SNR = 0.02 × SFR as inferred from the Starburst 99 models using a constant star formation episode (Leitherer et al. 1999).

One of the interesting results obtained from our new *N*-band data is establishing the photometric and the spectroscopic differences between the northern and the southern nuclei, which cannot be explained simply by differences in dust obscuration. Since the starburst activity in these nuclei must have been triggered by the merger of two progenitors, the age of the starbursts is likely to be comparable, but other physical parameters could be different in the two separate merging parent galaxies.

X-ray, optical and near-IR observations are indicative of a highly obscured southern nucleus which is completely hidden at visible wavelengths but which becomes increasingly prominent in the near-IR. The brightnesses of the two peaks are comparable at ∼4 μm and at radio wavelengths. Hence, it might be anticipated that in the mid-IR, where extinction becomes negligible, the two nuclei would also have similar flux levels. But this is not observed. Instead, we find that the northern nucleus exhibits excess continuum emission at wavelengths $\gtrsim$10 μm when compared with the southern nucleus and with our model SEDs.

Interestingly, a similar behaviour was found by Alonso-Herrero et al. (2006) when comparing the 8 μm and Paα emission from a sample of LIRG nuclei, including NGC 3256. While the northern nucleus shows a high-8 μm/Paα ratio, as was also seen in other LIRGs, the lower 8 μm/Paα value of the southern nucleus is consistent with the ratios observed in H II regions. Alonso-Herrero et al. (2006) explain this difference by the presence of large-scale diffuse emission, which is characterized by strong PAH features in the mid-IR. As can be seen in Table 3, for NGC 3256, the equivalent width (EW) of the 11.3 μm PAH feature changes at most by a factor of 3 between small (11.2–1.3 arcsec) and large (10.5–24 arcsec) apertures, while the line fluxes are greater by a factor of ∼6. This suggests that the fractional increase in the continuum flux is also substantial (factor of $\gtrsim$2). In addition, the data presented in Figs 4 and 5 suggest that a significant fraction of the excess mid-IR flux is due to continuum emission produced by warm dust, heated in situ by the starburst itself.

Using *Spitzer* IRS observations, Brandl et al. (2006) has quantified the continuum fluxes at 6, 15 and 30 μm for a sample of starburst galaxies, including NGC 3256. Brandl's observations show that the flux ratio $F_{6\,\mu m}/F_{15\,\mu m} = 0.14$ determined for NGC 3256 is significantly lower than the average $\langle F_{6\,\mu m}/F_{15\,\mu m}\rangle = 0.26$ found for their starburst sample. As we have shown, the northern nucleus is more luminous than the southern nucleus by a factor of ∼2 at 5.8 μm, while at 15 μm the flux should be dominated by the northern

nucleus. Indeed, using the best-fitting SEDs, we find $F_{6\ \mu m}/F_{15\ \mu m} = 1.2$ for the southern nucleus, while for the northern nucleus we adopt the value tabulated from the IRS spectrum. The full range of observed flux ratios in Brandl's sample is ∼0.1–0.6, which probably reflects the range in starburst conditions, such as age and dust properties. We find that the nuclei in NGC 3256 are representative of the two extremes of this distribution, but are found in the same central region of a single galaxy.

Finally, we compare the 10.5 μm and (unabsorbed, 2–10 keV) X-ray fluxes for both nuclei with the correlation derived by Krabbe, Böker & Maiolino (2001) using *N*-band MANIAC observations. The X-ray fluxes correspond to 9×10^{-17} and 4×10^{-17} W m^{-2} (Lira et al. 2002), while the 10.5 μm fluxes ($\Delta\lambda = 5$ μm, assuming the best-fitting SEDs) are ∼400 and ∼40 mJy, respectively. It is found that both nuclei are X-ray deficient given their *N*-band photometry. In particular, because of its high-mid-IR flux, the northern nucleus becomes a clear outlier in this correlation. But as shown by Krabbe's work, this is not the case for NGC 3256 when the fluxes are integrated over a large region, implying that the correlation holds for global starburst properties, but individual regions can show a much wider range of properties. In particular, our work shows that *in situ* dust heating in LIRGs, whose emission can dominate the mid-IR emission, can be confined to very compact (few hundred-pc scale) regions.

ACKNOWLEDGMENTS

PL and VG are grateful of support by the Fondecyt project No. 1040719. We would like to thank Dr. B. Brandl for kindly supplying the IRS observations. We also wish to thank an anonymous referee for useful comments.

REFERENCES

Alexander D. M., Bauer F., Chapman S., Smail I., Blain A., Brandt W., Ivision R. J., 2005, ApJ, 632, 736
Alonso-Herrero A., Colina L., Packham C., Diaz-Santos T., Rieke G., Radomski J., Telesco C. M., 2006, ApJ, 652, L83
Böeker T., Storey J. W. V., Krabbe A., Lehmann T., 1997, PASP, 109, 827
Brandl B. R. et al., 2006, ApJ 653, 1129
Calzetti D., Armus L., Bohlin R. C., Kinney A. L., Koornneef J., Storchi-Bergmann T., 2000, ApJ, 533, 682
Désert F.-X., Boulanger F., Puget J. L., 1990, A&A, 237, 215
Dopita M. A. et al., 2005, ApJ, 619, 755
Doyon R., Joseph R. D., Wright G. S., 1994, ApJ, 421, 101
Draine B. T., 2003, ARA&A, 41, 241
Galliano E., Alloin D., Pantin E., Lagage P. O., Marco O., 2005, A&A, 438, 803
Kotilainen J. K., Moorwood A. F. M., Ward M. J., Forber D. A., 1996, A&A, 305, 107
Krabbe A., Böker T., Maiolino R., 2001, ApJ, 557, 626
Laurent O., Mirabel I. F., Charmandaris V., Gallais P., Madden S. C., Sauvage M., Vigroux L., Cesarsky C., 2000, A&A, 359, 887
Le Floc'h E., Mirabel I. F., Laurent O., Charmandaris V., Gallais P., Sauvage M., Vigroux L., Cesarsky C., A&A, 2001, 367, 487
Leitherer C. et al., 1999, ApJS, 123, 3
Lípari S., Díaz R., Taniguchi Y., Terlevich R., Dottori H., Carranza G., 2000, AJ, 120, 645
Lira P., Ward M., Zezas A., Alonso-Herrero A., Ueno S., 2002, MNRAS, 330, 259
Martín-Hernández N. L., Schaerer D., Peeters E., Tielens A. G. G. M., Sauvage M., 2006, A&A, 455, 853
Moorwood A. F. M., Oliva E., 1994, ApJ, 429, 602
Moran E. C., Lehnert M. D., Helfand D. J., 1999, ApJ, 526, 649
Norris R. P., Forbes D. A., 1995, ApJ, 446, 594
Peeters E., Spoon H. W. W., Tielens A. G. G. M., 2004, ApJ, 613, 986
Ptak A., Colbert E., van der Marel R. P., Roye E., Heckman T., Towne B., 2006, ApJS, 166, 154
Rigopoulou D. et al., 1996, A&A, 315, L125
Sanders D. B., Egami E., Lípari S., Mirabel I. F., Soifer B. T., 1995, AJ, 110, 1993
Siebenmorgen R., Krügel E., Spoon H. W. W., 2004, A&A, 414, 123
Sturm E., Lutz D., Tran D., Feuchtgruber H., Genzel R., Kunze D., Moorwood A. F. M., Thornley M. D., 2000, A&A, 358, 481
Taylor-Mager V. A., Conselice C. J., Windhorst R. A., Jansen R. A., 2007, ApJ, 659, 162
Verma A., Lutz D., Sturm E., Sternberg A., Genzel R., Vacca W., 2003, A&A, 403, 829
Zepf S. E., Ashman K. M., English J., Freeman K. C., Sharples R. M., 1999, AJ, 118, 752

This paper has been typeset from a TEX/LATEX file prepared by the author.